Research Square

Preprints are preliminary reports that have not undergone peer review.
They should not be considered conclusive, used to inform clinical practice,
or referenced by the media as validated information.

Stability-Based Optimization of Planar Quiet Wind Tunnel Nozzles: Two-Dimensional Design and Three-Dimensional Assessment

Alberto Testa

alberto.testa@vki.ac.be

Von Karman Institute for Fluid Dynamics

Pierre Schrooyen

Von Karman Institute for Fluid Dynamics

Johan Steelant

European Space Research and Technology Centre

Thierry Magin

Université Libre de Bruxelles

Guillaume Grossir

Von Karman Institute for Fluid Dynamics

Research Article

Keywords: quiet wind tunnels, boundary-layer stability, laminar–turbulent transition, linear stability theory, Bayesian optimization, three-dimensional effects

Posted Date: July 10th, 2026

DOI: https://doi.org/10.21203/rs.3.rs-10225058/v1

License: This work is licensed under a Creative Commons Attribution 4.0 International License.
Read Full License

Additional Declarations: Competing interest reported. Competing interests: Author J. Steelant serves as a Managing Editor of CEAS Space Journal. Johan Steelant was not involved in the editorial handling, peer review, or decision-making process for this manuscript. The remaining authors declare no competing interests.

Stability-Based Optimization of Planar Quiet Wind Tunnel Nozzles: Two-Dimensional Design and Three-Dimensional Assessment

Alberto Testa[1,2*], Pierre Schrooyen[1], Johan Steelant[3], Thierry Magin[2], Guillaume Grossir[1*]

[1*]Aeronautics & Aerospace Department, von Karman Institute for Fluid Dynamics, Rhode-Saint-Genèse, 1640, Belgium.
[2]Department of Aero-Thermo Mechanics, Université Libre de Bruxelles, Bruxelles, 1050, Belgium.
[3]Flight Vehicles and Aerothermodynamics Engineering Section, European Space Research and Technology Centre, Noordwijk, 2201, The Netherlands.

*Corresponding author(s). E-mail(s): alberto.testa@vki.ac.be; guillaume.grossir@vki.ac.be;
Contributing authors: pierre.schrooyen@vki.ac.be; johan.steelant@esa.int; thierry.magin@ulb.be;

Abstract

The design of quiet supersonic nozzles is commonly performed within a two-dimensional framework, assuming either axisymmetric configurations or spanwise-homogeneous planar flows. While this approximation is appropriate for axisymmetric geometries, planar nozzles are inherently three-dimensional due to the presence of lateral sidewalls. This work assesses the robustness of two-dimensional optimization strategies through a combined two and three-dimensional stability analysis. A stability-based optimization, exploiting linear stability theories, is first conducted in a two-dimensional framework targeting the suppression of first-mode and Görtler instabilities. The resulting configurations are then evaluated using a three-dimensional laminar base flow including sidewall effects. The results show that two-dimensional predictions remain accurate along the top wall, whereas sidewall regions exhibit additional instability mechanisms induced by secondary flow mechanisms generating crossflow-type disturbances not captured in the planar model. Wall temperature control is shown to mitigate

instability growth on the top-wall and partially reduce crossflow amplification along the sidewalls. These findings demonstrate that, although two-dimensional optimization is effective for top-wall stability, three-dimensional effects must be considered for reliable nozzle design.

Keywords: quiet wind tunnels, boundary-layer stability, laminar–turbulent transition, linear stability theory, Bayesian optimization, three-dimensional effects

1 Introduction

Conventional high-speed wind tunnels remain a fundamental tool for investigating Boundary Layer (BL) transition in supersonic and hypersonic flows. However, their ability to reproduce flight-representative conditions is inherently limited by elevated freestream disturbance levels, primarily originating from turbulence-induced acoustic radiation within nozzle-wall boundary layers [1–4]. These disturbances can significantly alter the natural transition process, affecting both the onset location and the underlying instability mechanisms [5]. As a result, the fidelity of ground-to-flight extrapolation is reduced, with direct implications for the prediction of aerodynamic performance [6], thermal loads [7], and internal propulsion system behavior. To overcome these limitations, the development of advanced quiet ground-based facilities has emerged as a cornerstone in high-speed aerothermodynamics [8]. By minimizing freestream disturbances, such facilities enable controlled investigations of natural transition mechanisms, and provide high-quality experimental data for the validation of numerical models across a wide range of flow regimes.

The concept of quiet wind tunnels emerged in the 1970s and 1980s through foundational work conducted at NASA. Beckwith and Holley [9] highlighted how concave wall curvature in supersonic and hypersonic nozzles can trigger Görtler instabilities [10–12], stressing the importance of shallow expansions and large curvature radii to minimize Görtler growth rates. Chen, Malik, and Beckwith [13] further investigated the role of both centrifugal and first-mode instabilities using experiments and Linear Stability Theory (LST)[14].

A major step forward was achieved through the work of Schneider [1, 15, 16], who synthesized previous findings into a comprehensive design methodology for quiet nozzles. His contributions guided the development of the BAM6QT facility at Purdue University and established key design principles, including tailored nozzle contour design, local throat heating followed by wall cooling [17], and nozzle convergent region boundary-layer suction, to maintain laminar wall conditions and suppress radiated disturbances [15]. These strategies have since become standard in quiet nozzle design.

More recently, Lakebrink et al. [18] built upon these concepts by coupling Computational Fluid Dynamics (CFD) with LST-based instability analysis, embedding the evaluations into a Kriging metamodel loop for design optimization [19]. Their work demonstrated that significant improvements in quiet performance can be achieved through stability-based geometry optimization. However, the computational demands

of full CFD simulations may reduce the practicality of this approach for rapid design iterations or broad parametric explorations.

A further step was recently provided by Lemarquand et al. [20], who employed global and resolvent analyses to characterise instability mechanisms in hypersonic wind-tunnel nozzles. This framework captures both non-parallel effects and instabilities associated with separated regions, while providing sensitivity information on the base flow and the regions most responsible for amplification. Although particularly powerful for optimization-oriented studies, its computational cost remains significant, motivating the development of reduced-order yet physically consistent methodologies that retain the essential stability physics while enabling efficient design iteration.

In this context, the present study builds upon a previously developed modular framework [21], which combines inviscid contour generation, viscous boundary-layer computation, and LST simulations within a fast and automated pipeline. In its original formulation, this approach was applied to axisymmetric configurations and shown to capture the dominant instability trends at a fraction of the computational cost of fully resolved Navier–Stokes-based approaches.

When applied to planar nozzles, however, this type of methodology relies on a fundamental simplification: the assumption of spanwise-homogeneous flow. In practice, planar configurations are inherently three-dimensional due to the presence of lateral sidewalls. The resulting anisotropic expansion, generated by expansion in the vertical direction without a corresponding expansion in the spanwise direction, introduces spanwise pressure gradients and secondary flow structures, which distort the boundary layer and may give rise to instability mechanisms that are absent in a two-dimensional description. Whether designs obtained under planar assumptions remain valid in the presence of these effects is therefore not obvious.

The objective of the present work is to address this question. A stability-based optimization is first carried out within a two-dimensional framework, combining geometric and thermal control to reduce the amplification of the dominant instability mechanisms. The resulting configurations are then re-evaluated using fully three-dimensional base flow simulations including sidewalls, and their stability characteristics are reassessed based on the corresponding boundary-layer profiles.

The analysis shows that two-dimensional predictions remain accurate along the top wall, while additional instability mechanisms arise along the sidewalls that are not captured in planar analyses, highlighting the limits of the optimization framework.

To support these findings, the paper is structured as follows. Section 2 introduces the two-dimensional computational framework for base flow generation and stability analysis. Section 3 presents the stability-based optimization setup, including the objective function and design variables. The optimization results are discussed in Section 4. Section 5 extends the analysis to three-dimensional configurations, evaluating the influence of sidewall effects on flow stability. Finally, Section 6 summarizes the main conclusions and outlines directions for future work.

2 Two-Dimensional Methodology Overview

This section presents the computational framework used for nozzle design and stability assessment. The methodology combines inviscid contour generation, viscous boundary-layer analysis, and LST simulations within a unified pipeline, enabling efficient evaluation of candidate configurations.

The approach builds upon a previously developed framework [21], here adapted and extended to support automated exploration of the design space within an optimization loop. The design pipeline is first described, followed by the Bayesian optimization strategy used to guide the search.

2.1 Design pipeline

Figure 1 presents the design pipeline used for high-fidelity evaluations within the optimization loop.

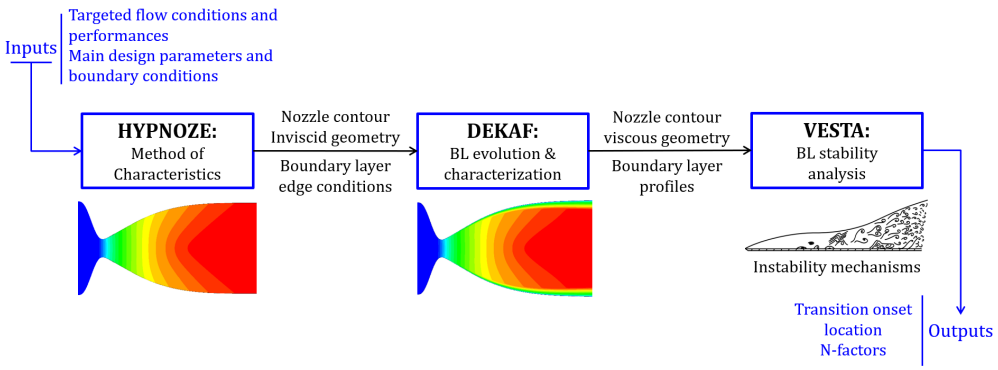


Fig. 1 Overview of the computational framework used for nozzle design and optimization.

The inviscid flow expansion and corresponding nozzle contour are computed using the HYPNOZE toolkit based on a set of geometric parameters and operating conditions (highlighted in red in Figure 2). These include the stagnation conditions (P_0, T_0), target exit Mach number (M_{exit}), throat half height (h^*), wall curvature at the throat (R_{C}), boundary-layer initialization location (x_{BL}), straightening length (X_{BC}), nozzle opening angle (ω), and wall temperature distribution $(T_{\text{w}}(x))$. The solution is obtained via a Method of Characteristics (MoC) formulation [22], providing both the nozzle geometry and the edge flow conditions along the wall.

The parameter x_{BL} defines the streamwise location at which the boundary layer is initialized, typically upstream of the throat to account for a hypothetical bleed suction system. The parameter X_{BC}, instead, represents the length of the straightening section in the divergent part of the nozzle and controls the transition from the radial flow region to the uniform parallel flow region.

The resulting contour and wall flow conditions are then provided as input to DEKAF [23], a compressible, laminar, marching boundary-layer solver. DEKAF computes velocity and thermodynamic profiles along the nozzle wall and provides integral quantities, such as the displacement thickness δ^*, which are used to account for viscous corrections to the effective geometry.

Although the wall temperature distribution $T_w(x)$ does not affect the inviscid contour generation, it plays a key role in the boundary-layer development and therefore in the viscous correction of the geometry. In the present framework, $T_w(x)$ is defined through a set of control points and interpolated using spline functions, enabling flexible definition of the thermal boundary condition during the optimization process.

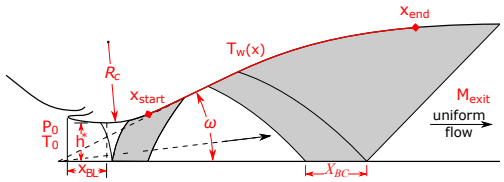


Fig. 2 Overview of the design input variables used in the pipeline, adapted from Sivells [24].

The boundary-layer profiles are subsequently analyzed using the von Karman Institute's (VKI) VESTA [25] toolkit, which applies local spatial LST [14, 26]. Under the assumption of locally parallel flow and small-amplitude disturbances, perturbations are expressed in normal-mode form as in Eq. 1:

$$q'(x, y, z, t) = \hat{q}(y)\, \exp\left(i\alpha x + i\beta z - i\omega_f t\right) \tag{1}$$

where $\alpha = \alpha_r + i\alpha_i$ is the complex streamwise wavenumber, β the spanwise wavenumber and ω_f is the angular frequency. The imaginary part $-\alpha_i$ represents the local spatial growth rate of the disturbance.

The LST analysis is performed over a range of frequencies and spanwise wavenumbers to identify, for each instability mechanism, the most amplified disturbances and their corresponding growth rates. The analysis considers the three primary instability mechanisms typically observed in nozzle flows [15, 18, 20]: namely the first-mode, the second-mode, and Görtler instabilities. Instability mechanisms inherently associated with three-dimensional boundary-layer structures, such as crossflow [27], cannot be captured within the present two-dimensional framework, as their development requires a fully three-dimensional baseflow. These effects are therefore addressed separately in Section 5.

Additional comparisons, presented in [21], with Linear Parabolized Stability Equations (LPSE) [28] have been performed to verify the local analysis methodology. In contrast to LST, which assumes locally parallel flow and represents disturbances using a normal-mode ansatz with a fixed streamwise wavenumber, LPSE accounts for the slow streamwise evolution of both the base flow and the disturbance. In this framework, perturbations are expressed as in Eq. 2:

$$q'(x,y,z,t) = \hat{q}(x,y)\,\exp\left(i\int \alpha(x)\,dx + i\beta z - i\omega_f t\right) \tag{2}$$

where both the disturbance amplitude $\hat{q}$ and the streamwise wavenumber α are allowed to vary with the streamwise coordinate.

The close agreement between LST and LPSE predictions, observed in previous study [21], indicates that non-parallel effects have a limited impact on instability growth under the present conditions, thereby supporting the use of LST for early-stage transition assessment.

Stability results are interpreted in terms of the N-factor, obtained from the e^N method [29, 30], defined in as:

$$N(x) = \ln\left(\frac{A(x)}{A(x_0)}\right) = \int_{x_0}^{x} -\alpha_i(\xi)\,d\xi \tag{3}$$

where $A(x)$ denotes the amplitude of the instability disturbance, and x_0 is the neutral point, i.e. the location where the streamwise growth rate becomes zero ($\alpha_i = 0$) and the disturbance first transitions from decay to amplification (with $\alpha_i < 0$ downstream of x_0). The N-factor thus represents the logarithmic amplification of the disturbance amplitude along the boundary layer.

Under the assumption of linear disturbance evolution, transition onset is estimated by comparison with a critical threshold, using the e^N method. For quiet high-speed wind tunnel applications, Chen et al. [13] established a reference value of $N_{\text{crit}} \approx 7.5$.

In addition, the quiet Reynolds number is evaluated based on the streamwise extent Δx of the region where the amplification remains below the critical threshold (see Figure 3), providing a quantitative measure of the achievable quiet core length.

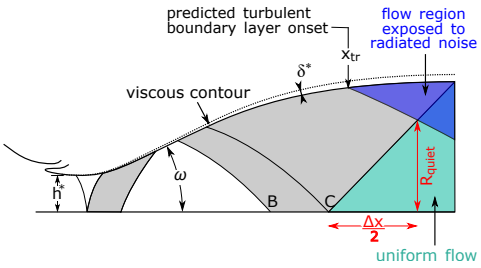


Fig. 3 Visualization of half of the quiet flow region (Δx) used to define the quiet Reynolds number.

The described methodology is directly applicable to both planar and axisymmetric nozzle configurations, provided that the governing equations of the Method of Characteristics, the boundary-layer formulation, and the associated coordinate system are adapted accordingly. Its modular structure enables efficient exploration of a wide range of design configurations.

Further details on the methodology, including viscous corrections and validation against literature data and Navier–Stokes simulations, are provided by Testa et al. [21].

2.2 Non-Intrusive Optimization Loop

The full design pipeline, HYPNOZE → DEKAF → VESTA, is embedded in a *Bayesian Optimization* (BO) [31] framework that treats the entire chain as a black-box function. This non-intrusive approach enables geometry optimization without the need for adjoint methods, manual differentiation, or solver modification. Given the relatively low dimensionality of the problem and the computational cost of each simulation (roughly one hour on a single core), Bayesian Optimization offers an ideal balance between accuracy and efficiency.

The optimization proceeds through the following stages, presented in Figure 4:

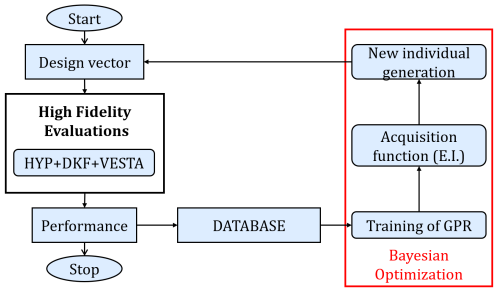


Fig. 4 Bayesian Optimization process flow chart.

1. **Design initialization (Start and Design vector):** The optimization begins with an initial set of nozzle geometries, sampled using Latin Hypercube Sampling (LHS) [32] to ensure broad coverage of the design space. Each design vector includes geometric and thermal parameters that define a candidate configuration.
2. **High-Fidelity evaluation (HYPNOZE + DEKAF + VESTA):** Each candidate is evaluated using the full simulation pipeline. This includes inviscid flow solution and nozzle contour generation (HYP), viscous corrections (DKF), and LST simulations (VESTA). The performance metrics—such as N-factor growth and quiet Reynolds number—are computed and stored.
3. **Database update (DATABASE):** Evaluation results are added to the design database, forming the training set for surrogate modeling.
4. **Surrogate model training (Learning):** A Gaussian Process Regression (GPR) [33] model is trained on the accumulated data. It provides predictions of performance metrics and quantifies uncertainty across the design space.
5. **Acquisition function (Expected Improvement):** The Expected Improvement (EI)[19] acquisition function guides the search by balancing *exploration* of uncertain regions and *exploitation* of promising designs. The next candidate is selected by maximizing EI.

6. **New candidate generation:** The selected design vector is passed to the simulation pipeline for evaluation, completing one optimization loop.
7. **Convergence check (Loop and Stop):** The process iterates, updating the GPR model, re-evaluating the acquisition function and generating new candidates, until an iteration number is reached.

The optimization framework is implemented in Python using `scikit-learn` for GPR and `scikit-optimize` for BO, enabling a flexible and reproducible implementation.

3 Optimization Framework

To evaluate the effectiveness of the proposed methodology, a planar supersonic nozzle ($M = 3.5$) is considered. The optimization aims to delay laminar-to-turbulent transition by minimizing the amplification of boundary-layer instabilities along the nozzle wall through the combined control of geometric and thermal boundary conditions. The analysis is conducted within a two-dimensional framework, consistent with standard design practice.

3.1 Objective Function

The N-factor method is a well-established approach for estimating BL transition onset and is commonly used to guide both experimental interpretation and numerical studies. In the context of quiet supersonic tunnels, a critical threshold of $N_{\text{crit}} = 7.5$ is assumed. [13]. This criterion provides a practical reference for assessing whether transition is likely to occur within the nozzle.

Given the freestream Mach number of $M = 3.5$ targeted in this study and the high quiet Reynolds ($Re_{\Delta x} = 20 \times 10^6$), the two primary instability mechanisms considered in the 2D analysis are:

- First-mode instabilities, which arise from viscous–inviscid interaction in the boundary layer and typically manifest as oblique waves, corresponding to disturbances with non-zero temporal frequency ($\omega_f \neq 0$) and spanwise wavenumber ($\beta \neq 0$);
- Görtler instabilities, arising in concave geometries and driven by centrifugal effects induced by wall curvature, and typically characterized by stationary ($\omega = 0$) streamwise-aligned vortical structures with finite spanwise wavenumber ($\beta \neq 0$).

Second-mode instabilities are not expected to be significant at this Mach number but are included in the analysis of each configuration for completeness.

Beckwith et al. [34] showed that in planar nozzles operating at $M = 3.5$, Görtler instabilities tend to dominate over first-mode disturbances. Transition assessment is performed using Schneider's [15] composite measure:

$$N_{\text{combined}} = \sqrt{N_{\text{1st}}^2 + N_{\text{2nd}}^2 + N_{\text{Gö}}^2}, \tag{4}$$

consistent with common quiet-nozzle practice, which combines the contributions of both mechanisms through an orthogonal formulation. For optimization, however,

the root-sum-square form reduces sensitivity to weak but nonzero amplification: for $0 < N \ll 1$, squaring further diminishes the contribution of that mechanism to the objective, even though such disturbances may still grow and can interact with other modes downstream. To avoid this limitation, a linear combination is introduced to define the objective function:

$$N_{\text{tot}} = N_{\text{1st}} + N_{\text{2nd}} + N_{\text{Gö}}, \tag{5}$$

which preserves the contribution of both mechanisms and provides a more responsive metric for optimization. The Bayesian optimization framework therefore minimizes the following cost-function:

$$J = N_{\text{tot}}, \tag{6}$$

while transition onset estimation is evaluated using the standard N_{combined} criterion, defined in Eq. 4.

Secondary engineering requirements are evaluated *a posteriori* and used to guide the final selection among the best-performing candidates. Specifically, we define a design as *feasible* if it satisfies the requirements listed below; the recommended optimal configuration reported in this work is the best-performing feasible design within the sampled set:

- **Geometric smoothness / manufacturability:** no curvature discontinuities and no localized contour irregularities after viscous correction.
- **Thermal realizability:** bounded wall-temperature gradients and no unrealistically sharp heating–cooling steps in $T_{\text{w}}(x)$.

3.2 Design Space and Design of Experiment definition

Starting from the complete set of parameters influencing nozzle geometry (illustrated in Figure 2), the design space was reduced to a subset of key variables in order to limit computational cost while preserving performance fidelity and physical relevance.

Stagnation conditions (P_0, T_0) were fixed according to the operational constraints of the VKI wind tunnels, reflecting realistic achievable operational conditions ($P_0 = 5$ bar, $T_0 = 290$ K). The boundary-layer start location (x_{BL}) and the throat curvature radius (R_{C}) were fixed according to literature guidelines to promote a well-developed boundary layer and maintain flow uniformity in the vicinity of the throat [16, 24].

Specifically, x_{BL} was placed one throat diameter upstream of the geometric throat to mimic the presence of a bleed lip, which would remove the incoming boundary layer from the contraction region. This allows a clean boundary layer to develop along the divergent section without requiring the full design of a bleed system at this stage. The wall curvature in the throat vicinity was set to $R_{\text{C}}/h^* = 20$, promoting a smooth and gradual expansion that helps suppress early curvature-driven instabilities, as recommended in previous studies [35].

The throat half-height h^* is set to 0.015 m to target a quiet Reynolds number of 20×10^6 while maintaining nozzle compactness and manufacturability. This value provides a consistent reference scale across the design space; however, the resulting quiet Reynolds number remains dependent on the boundary-layer development and is therefore verified a posteriori through stability analysis.

The remaining free design variables for the optimization are the maximum opening angle ω, the non-dimensional length X_{BC}, and the wall temperature distribution $T_{\mathrm{w}}(x)$, each detailed in the subsequent subsections. These variables define the objective function as

$$J = \min\left(N_{\mathrm{tot}}(\omega, X_{\mathrm{BC}}, T_{\mathrm{w}}(x))\right). \tag{7}$$

3.2.1 Straightening length (X_{BC})

The non-dimensional length between design points B and C, X_{BC} (Fig. 3), defines the transition region between the radial-flow and uniform-flow sections. It is computed using Sivells' methodology [36], which provides lower and upper bounds ($X_{BC,\mathrm{min}}$, $X_{BC,\mathrm{max}}$) such that the Mach number at point B lies between 75% and 80% of the nozzle exit value. To preserve flow quality and avoid expansion discontinuities, X_{BC} is defined through a normalized design variable $X_{\mathrm{BC},\%}$ ranging from 0 to 100%:

$$X_{\mathrm{BC}} = X_{\mathrm{BC,min}} + (X_{\mathrm{BC,max}} - X_{\mathrm{BC,min}}) \cdot X_{B\mathrm{BC},\%} \tag{8}$$

This formulation enables a smooth variation of the expansion length while staying within physically meaningful bounds.

3.2.2 Nozzle opening angle (ω)

The maximum opening angle plays a critical role in the amplification of centrifugal instabilities (Görtler modes). As shown in previous studies [13], lower values of ω promote flow stability by increasing the wall radius of curvature and thereby reducing centrifugal effects. In this study, ω was constrained between 2° and 4°, with the lower bound selected to prevent impractically long nozzle geometries.

3.2.3 Wall Temperature Distribution ($T_{\mathrm{w}}(x)$)

The temperature distribution is parameterized using three intermediate control points and a fourth at the nozzle exit. The location of each point is defined as a percentage of the nozzle length (x_i/L), and the temperature profile is obtained by interpolation using a shape-preserving piecewise cubic Hermite polynomial. The temperature at each control point ranges from 290 K to 350 K, a range that is both practically achievable with simple heating systems and low enough to avoid deformation or manufacturability issues. Wall temperature plays a pivotal role in boundary-layer stability, particularly near the throat region where the boundary layer is most sensitive to disturbance amplification. In this regard, targeted heating has been shown to effectively suppress first-mode growth [15]. In particular, Demetriades [17] demonstrated that local surface heating near the throat stabilizes the laminar boundary layer by shifting the onset of transition downstream, thereby providing a control strategy with substantial benefits for quiet nozzle performance.

Table 1 summarizes all the design variables along with their upper and lower bounds. An initial Design of Experiments (DoE) of 64 individuals was generated using LHS to ensure uniform coverage of the defined design space.

Table 1 Design of Experiments (DoE) parameter ranges

Parameter	Min	Max
ω [deg]	2.0	4.0
$X_{\mathrm{BC},\%}$ [%]	0	100
x_1/L [%]	20	40
x_2/L [%]	45	70
x_3/L [%]	75	95
T_1 [K]	290	350
T_2 [K]	290	350
T_3 [K]	290	350
T_4 [K]	290	350

3.3 Reference Design Identification

A reference configuration was defined to represent a baseline, non-optimized nozzle design. This case assumes a constant wall temperature of 290 K and uses mid-range values for all geometric parameters. It serves as a benchmark for evaluating the relative performance improvements achieved through optimization.

The reference nozzle main design parameters, are summarized in Table 2.

Table 2 Reference nozzle design parameters

Parameter	Value	Unit
M_{exit}	3.5	–
P_0	5	bar
T_0	290	K
ω	3.0	deg
h^*	0.015	m
$X_{\mathrm{BC},\%}$	50	%
R_{C}/h^*	20	–
x_{BL}	$-2\,h^*$	m
$T_{\mathrm{w}}(x)$	300	K

Boundary-layer transition predictions based on LST are shown in Figure 5. The first-mode instability was analyzed over a frequency range of 1 to 6 kHz, while the Görtler instability was evaluated over a discrete range of spanwise modes corresponding to $N_{\mathrm{waves}} \in [20, 150]$ wavelengths across the nozzle width $W = 0.1$ m. The corresponding spanwise wavenumber is defined as

$$\beta = \frac{2\pi N_{\mathrm{waves}}}{W},$$

where each wavelength corresponds to a counter-rotating pair of Görtler vortices. The plot compares the amplification of each mode and their combination, showing that

the combined N-factor exceeds the critical threshold and therefore estimates transition within the nozzle, reducing thus the quiet Reynolds number ($Re_{\Delta x}$).

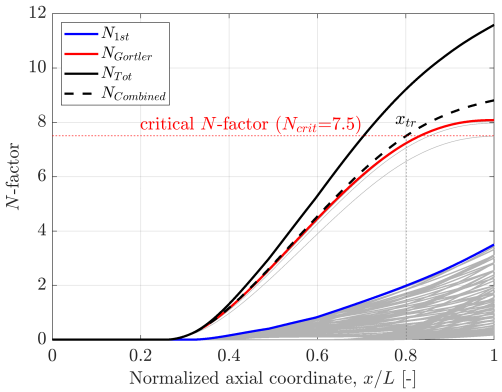


Fig. 5 N-factor evolution from LST for the reference configuration. Individual mode contributions, combined and total prediction are shown (N_{Combined} from Eq. 4, used to define if transition occurs and N_{Tot} from Eq. 5, used as optimization metric term). The second-mode instability does not arise under the present flow conditions.

As expected, the second mode instability in this configuration is not excited. The corresponding reference geometry and transition onset location is shown in Figure 6, where the transition point—identified by a blue diamond—marks the streamwise location at which the combined N-factor exceeds the critical value. From this point onward, disturbances begin to propagate into the core flow along characteristic lines governed by the local Mach angle, as determined by the edge Mach number. This limits the extent of the quiet region and may lead to contamination of the test section with acoustic noise.

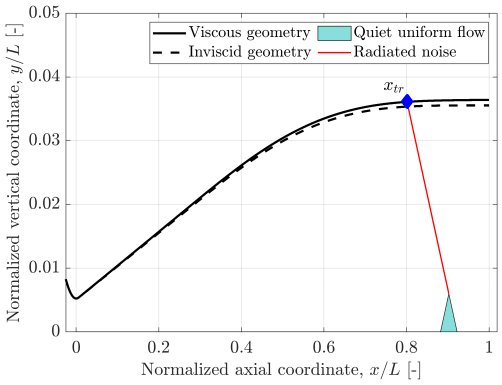


Fig. 6 Reference nozzle geometry (vertically stretched for enhanced visibility). Predicted transition location based on combined N-factor. Boundary-layer thickness and transition onset are indicated.

The resulting quiet Reynolds number for the reference configuration ($3.3 \cdot 10^6$) falls

significantly below the desired lower bound target of $20 \cdot 10^6$, reinforcing the need for geometry optimization and active thermal control strategies to delay transition and extend the quiet flow region.

4 Optimization Results

A total of 150 optimization iterations were performed within the BO loop. The accuracy of the surrogate model was assessed using Leave-One-Out (LOO) cross-validation [37]. In this framework, each sample is predicted using a surrogate model constructed from all remaining data points, providing an estimate of the model's generalization capability over the explored design space.

For the objective function, defined as the total N-factor at the nozzle exit (N_{tot}), the LOO analysis yielded a coefficient of determination (R^2) equal to 0.9736, indicating that the surrogate captures over 97% of the variance in the high-fidelity evaluations. This strong predictive performance is illustrated in Figure 7, where the predicted values closely align with the diagonal, demonstrating excellent agreement with the reference data.

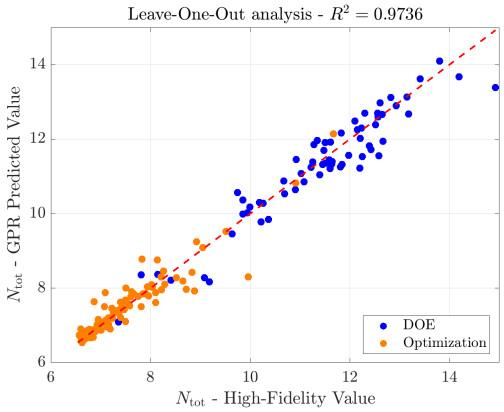


Fig. 7 Leave-One-Out analysis for the surrogate model built for supersonic quiet nozzle design

4.1 Influence of Design Parameters on Optimization

Figure 8 presents the distribution of all sampled configurations, including both the initial design of experiments and the subsequent optimization iterations, using a parallel coordinate representation. The objective value (N_{tot}) is used to color the trajectories, with darker shades corresponding to lower amplification levels. A clear clustering of low N_{tot} configurations can be observed, indicating convergence toward a restricted region of the design space, where only specific combinations of geometric and thermal parameters lead to reduced instability amplification.

These clustered patterns suggest that specific geometric trends consistently lead to lower instability levels. To better understand the physical mechanisms behind these optimal solutions, each key geometric parameter is examined individually below.

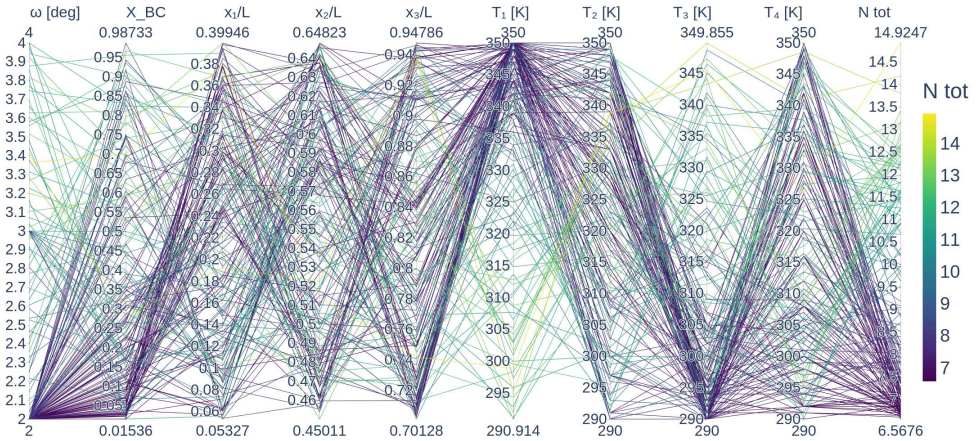


Fig. 8 Parallel coordinate plot showing the optimization trajectories.

- Nozzle opening angle (ω): Optimal solutions consistently lie at the lower bound of the allowed range ($\approx 2^\circ$), confirming the stabilizing role of shallow expansions. Lower values of ω increase the wall radius of curvature during the expansion, thereby reducing the local Görtler number and the associated centrifugal instability growth.
- Straightening length (X_{BC}): High-performing configurations exhibit low X_{BC} values, corresponding to a shorter extent of the concave flow region. This reduction appears to limit the development of concave-flow instabilities. The clustering near the lower bound suggests a saturation trend, motivating future exploration beyond the current limits.
- Wall temperature distribution ($T_{\mathrm{w}}(x)$): The wall temperature distribution is parameterized by control points: x_1, x_2 and x_3 define the spatial locations, while T_1 through T_4 define the imposed temperatures at those points and at the nozzle exit (x_4).
  Key insights include:
  - Location of control points (x_1/L, x_2/L, x_3/L): No dominant trend emerged; the ranges were pre-constrained within defined nozzle zones, making the temperature values more impactful than their exact locations.
  - High temperatures near the throat (T_1, T_2): Elevated values in the throat region correlate with improved performance. This stabilizes early-stage first-mode waves, consistent with prior studies [15].
  - Strong cooling at T_3: All top-performing designs exhibit a pronounced temperature drop at T_3, indicating a critical region where wall cooling reduces the amplification of first-mode instabilities. This behavior is consistent with literature observations, as cooling alters the boundary-layer, effectively weakening or shifting the inflectional region associated with first-mode amplification.

– Competing influence of T_4 (exit temperature): Increasing the terminal wall temperature promotes boundary-layer thickening and thus increases the displacement effect on the inviscid contour. In the present case, the resulting viscous correction modifies the effective wall geometry, locally shifting it from concave to convex and thereby attenuating Görtler amplification. At the same time, higher wall temperatures tend to destabilize first-mode disturbances. Consequently, T_4 introduces a trade-off between instability mechanisms, and its net effect depends on the relative balance of these competing trends.

To further support these findings, a global sensitivity analysis based on Sobol's indices [38] was conducted on the trained surrogate model. Figure 9 displays both the first-order (S_1) and total-order (S_T) indices. The results confirm the dominant influence of T_1, T_3 and ω, in agreement with the physical mechanisms outlined above. Notably, the difference between S_1 and S_T for T_2 and x_3 indicates the presence of strong parameter interactions.

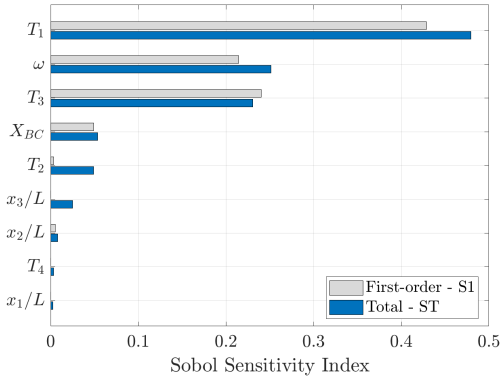


Fig. 9 Sensitivity analysis of design parameters using variance based Sobol methodology.

To complement the Sobol sensitivity analysis, Self-Organizing Maps (SOMs) [39] were employed as an unsupervised clustering technique to visualize high-dimensional patterns in the optimized dataset (see Figure 10). The SOM projects the parameter space onto a two-dimensional lattice, highlighting parameter interdependence and convergence pathways across the BO iterations.

The SOM visualization confirms trends already observed in the parallel coordinate plots and Sobol analysis:

- Regions of high performance are clearly localized and clustered on the SOM map for low ω and sharp temperature drops from high T_1 to low T_3.
- Parameters like x_1–x_3 and T_4 exhibit more uniform distribution across the map, further supporting their lower sensitivity.

Together, the combined use of GPR modeling, BO-driven sampling, Sobol analysis and SOM visualization offers a multi-perspective view of the optimization landscape,

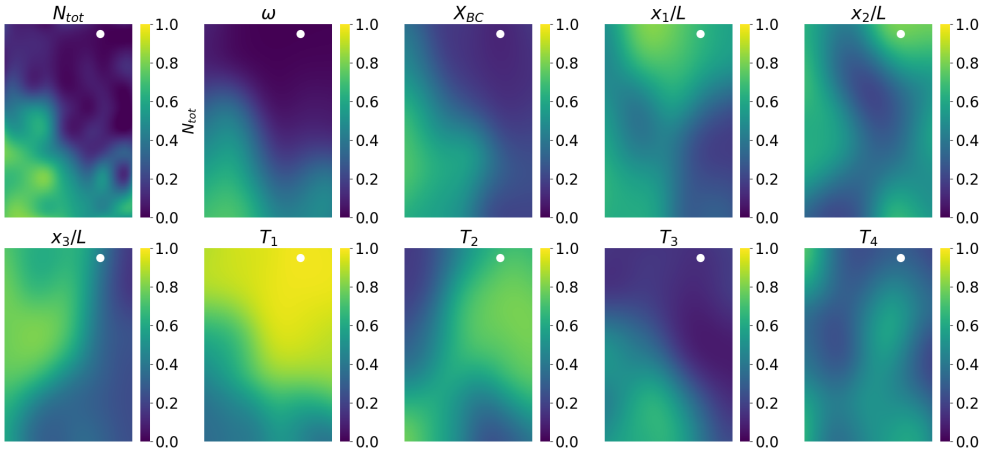


Fig. 10 Self-Organizing-Maps, all values are nondimensionalized within their operational defined bounds. White dot representing optimal individual.

enabling both quantitative sensitivity assessment and intuitive pattern recognition across high-dimensional parameter spaces.

An important observation is that the best individuals (i.e., with lowest N_{Tot}-factor envelope) do not exhibit transition within the nozzle, hence $N_{\mathrm{Combined}} < 7.5$, implying that the selected parameter combinations succeed in maintaining laminar flow throughout the contour. These configurations should therefore be favored in quiet wind tunnel applications.

4.2 Analysis of Optimal Design

The optimization process converges to a narrow range of high-performing solutions, indicating a well-defined optimum within the explored design space. Although several candidates exhibit comparable objective function values, differences in their thermal layouts lead to distinct stability behaviors. Among these, configuration IT048 is identified as the best candidate recalling the requirements presented in Section 3.1 and is selected for further analysis. Its selection is guided not only by its final integrated N-factor, which remains below the transition threshold, but also by its local stability characteristics, as it achieves a favorable redistribution of instability amplification along the nozzle, limiting the overlap between competing mechanisms.

Table 3 summarizes the corresponding design parameters. The associated wall temperature distribution is shown in Figure 11, highlighting a pronounced temperature drop downstream of approximately 30% of the nozzle length, followed by a slight increase toward the exit. This distribution reflects the role of localized cooling in controlling instability amplification.

The LST stability results of the selected configuration are reported in Figures 12 and 13, which respectively show the N-factor evolution and the corresponding local growth rates for the dominant instability mechanisms. The configuration maintains

Table 3 Optimal design parameters (IT048)

Parameter	Value	Unit
ω	2.0	deg
$X_{BC,\%}$	3	%
x_1/L	32	%
x_2/L	51	%
x_3/L	94	%
T_1	350	K
T_2	333	K
T_3	292	K
T_4	296	K
N_{tot}	6.62	–

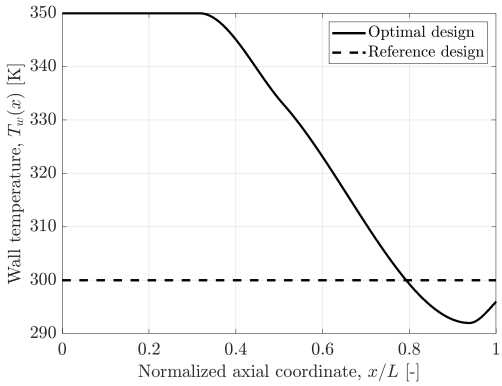


Fig. 11 Comparison between the wall temperature distribution of the selected optimal configuration (IT048) and the constant distribution of the reference design.

subcritical amplification levels throughout the nozzle, ensuring that transition is not expected using LST coupled with e^N method.

As shown in Figure 13, IT048 achieves a clear separation between the regions of peak amplification of the two mechanisms. While Görtler instability is primarily governed by the geometric expansion, the tailored wall temperature distribution reduces first-mode amplification in the same region. This limits the magnitude of $\alpha_{i,\text{Tot}}$, defined as the sum of the growth rates contribution from both modes, thereby reducing the potential for strong concurrent growth and increasing the overall robustness of the configuration.

Although the present analysis is linear (LST) and therefore does not model nonlinear coupling explicitly, the spatial overlap of strong amplification regions can be interpreted as a practical indicator of multi-mechanism transition scenarios. In the reference configuration, first-mode growth extends into the concave-curvature region where Görtler modes also amplify. In contrast, IT048 reduces this coexistence by shifting and weakening first-mode growth in the region of strongest curvature-driven amplification. This reduces the likelihood that competing mechanisms reach significant amplitudes simultaneously.

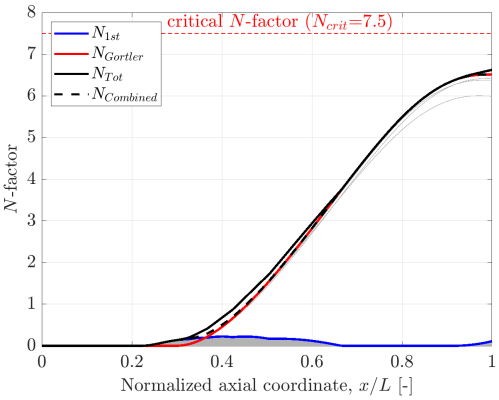


Fig. 12 N-factor evolution from LST for the optimal design (IT048). Individual mode contributions, combined and total prediction are shown.

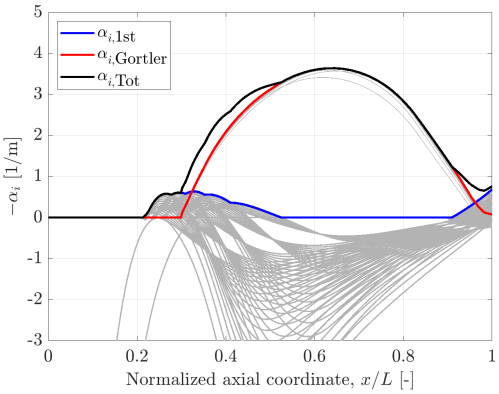


Fig. 13 Growth rate evolution from LST for the optimal design (IT048). Individual mode contributions and total prediction are shown.

5 Three-Dimensional Baseflow and Stability Assessment

The two-dimensional optimization results presented in the previous section demonstrate that appropriate combinations of geometric parameters and wall temperature distributions can effectively tackle first-mode and Görtler instabilities along the nozzle wall. However, these results are obtained under the assumption of a 2D infinite span flow and therefore do not account for the inherently three-dimensional nature of planar nozzle configurations.

To evaluate the robustness of the optimized designs under more realistic conditions, the flow is recomputed using three-dimensional CFD simulations including lateral sidewalls. Both the reference and optimized configurations are considered, enabling a direct assessment of the extent to which two-dimensional predictions remain valid when spanwise confinement effects are introduced.

The inclusion of straight sidewalls induces anisotropic expansion, as the nozzle expands in the vertical direction while no corresponding expansion occurs in the spanwise direction. This results in the development of secondary flow structures within the boundary layer. These features are expected to modify the local stability characteristics and may give rise to additional instability mechanisms that are not captured in the planar framework. The following sections investigate these effects through combined base flow analysis and stability computations.

5.1 Three-Dimensional Base flow Generation

A steady three-dimensional base flow is computed using the commercial CFD++ solver [40], considering the extrusion of the two-dimensional planar geometry and explicitly including lateral sidewalls. The simulation setup preserves the inlet conditions, thermodynamic assumptions, and boundary-layer start location (x_{BL}, defined in Table 2 as one throat height upstream of the throat), ensuring consistency with the two-dimensional analysis.

The computational domain consists of a quarter of the full geometry, exploiting two symmetry planes. It includes a reservoir conditions inlet, two viscous walls (top wall and sidewall, with either constant temperature or optimized temperature distribution), and a supersonic outlet.

The computational grid is generated using a Laplacian grid generator developed at VKI, in which displacement-thickness predictions from DEKAF are used to define the boundary-layer thickness and ensure its proper growth within the mesh. This approach ensures a boundary-layer-resolved grid with near-wall orthogonality along the entire expansion region, while allowing independent control of streamwise and wall-normal resolution to accurately capture boundary-layer development for subsequent stability analysis. In the fine mesh configuration, both top-wall and sidewall boundary layers are resolved with approximately 150 points in the wall-normal direction. To quantify numerical sensitivity of the three-dimensional base flow and of the stability metrics extracted from it, a grid refinement study was performed using a coarser mesh with reduced wall-normal point density in the boundary-layer region, while preserving the same topology and near-wall clustering strategy. Stability-relevant quantity, such as N factor evolution, is compared across meshes and showed limited grid-induced variation, supporting the grid adequacy for the stability analyses reported in the following sections. As a verification metric for stability extraction, Fig. 14 compares the envelope $N(x)$ obtained from profiles extracted along the wall in the spanwise symmetry plane for the coarse and baseline meshes. Differences remain limited (e.g., $\Delta N_{\mathrm{G\ddot{o}}} = 0.02$, $\Delta N_{1\mathrm{st}} = 0.3$), supporting use of the baseline mesh for the following analyses.

Verification of the three-dimensional base flow against the two-dimensional solution is performed on symmetry plane through comparisons of boundary-layer profiles and axis conditions (see Figures 15, 16, 17). While good agreement is observed near the inlet, deviations arise downstream of the nozzle inflection point, where the flow departs from the ideal two-dimensional expansion.

These deviations are directly linked to the presence of sidewalls. While the nozzle expands in the vertical direction, no corresponding expansion occurs in the spanwise

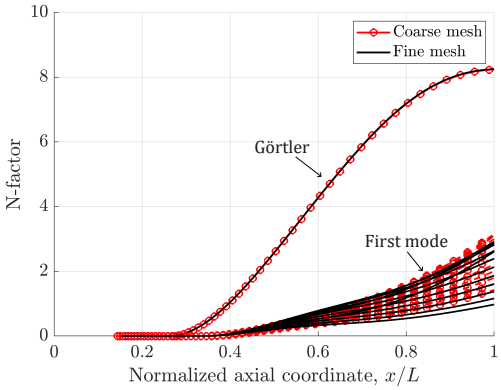


Fig. 14 N-factor evolution for symmetry plane top wall of both Görtler and first mode in coarse and fine meshes.

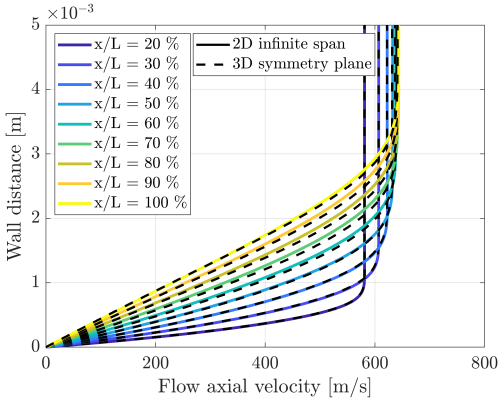


Fig. 15 Boundary-layer profiles of axial velocity U as a function of wall-normal distance in the symmetry plane of the nozzle. Comparison between the 2D infinite span methodology and the symmetry-plane solution from the 3D CFD base flow for the reference case.

direction, leading to anisotropic expansion. This leads to a non-uniform pressure distribution across the cross-section, particularly in the sidewall regions, driving secondary flow within the boundary layers. This mechanism has been experimentally observed by Sabnis et al. [41]. A schematic adapted from their work is shown in Figure 18.

The flow features observed in the present simulations are in direct agreement with the mechanism illustrated in Figure 18. This is confirmed by the three-dimensional base flow visualization shown in Figure 19, where a sequence of boundary-layer profiles extracted along the nozzle wall highlights the progressive deformation of the sidewall boundary layer.

In particular, the low-momentum region of the boundary layer is displaced toward the centerline under the effect of the spanwise pressure gradient, while corner vortical structures develop and intensify downstream of the inflection region. These structures induce a downward motion of fluid in the sidewall boundary layer, consistent with the lift-up mechanism described in the literature.

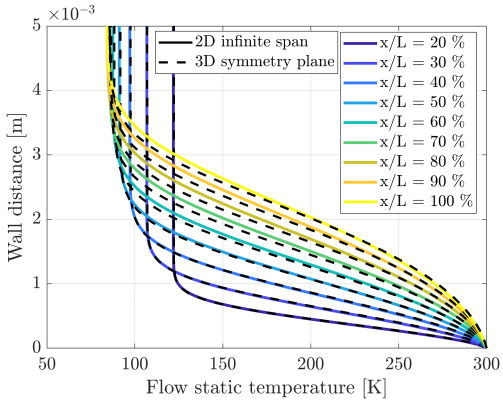


Fig. 16 Boundary-layer profiles of static temperature T as a function of wall-normal distance in the symmetry plane of the nozzle. Comparison between the 2D infinite span methodology and the symmetry-plane solution from the 3D CFD base flow for the reference case.

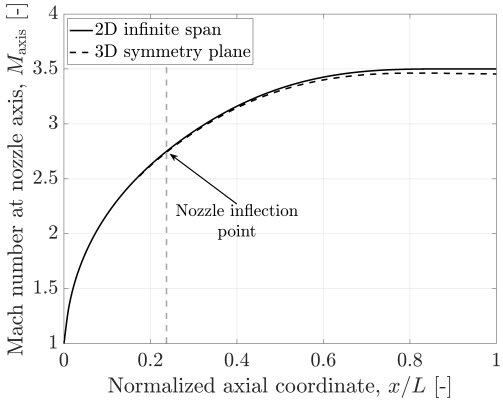


Fig. 17 Mach number evolution along the nozzle axis. Comparison between the 2D infinite-span methodology and the symmetry-plane solution from the 3D CFD base flow.

As a result, even geometries optimized under 2D infinite span assumptions develop a three-dimensional base flow characterized by secondary flow mechanisms in the boundary-layer region. These effects are expected to modify the stability characteristics by introducing cross-stream velocity components and potentially enabling crossflow-type instabilities [27] along the sidewalls, which are absent in the infinite span two-dimensional framework.

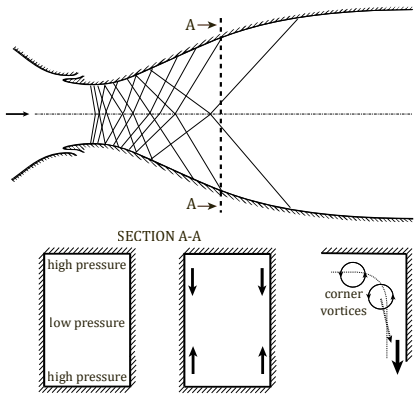


Fig. 18 Schematic of sidewall-induced secondary flows in the nozzle, showing the characteristic lines evolution, resulting cross-sectional pressure gradients, and the development of corner vortex structures. Adapted from [41].

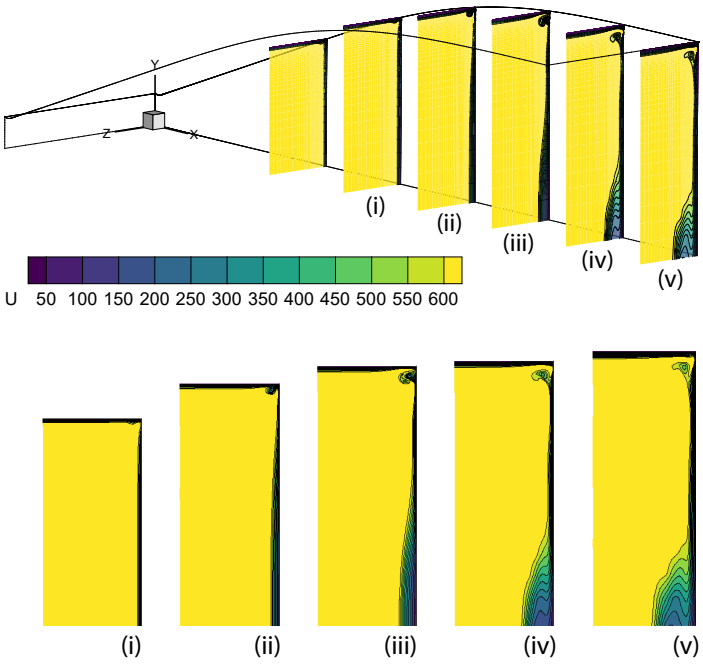


Fig. 19 CFD-based visualization of the sidewall-induced secondary flows introduced in Fig. 18 for the reference case geometry. Streamwise velocity contours on successive cross-sections illustrate the progressive development of corner vortices and the associated redistribution of low-momentum region (BL) toward the centerline.

5.2 Emergence of Additional Instability Mechanisms

As established in the two-dimensional analysis, instability dynamics at the present Mach number are primarily governed by first-mode disturbances and curvature-induced Görtler mechanisms, while second-mode instabilities remain negligible.

The three-dimensional base flow introduces secondary flow mechanisms in the boundary-layer structure, particularly along the sidewalls where secondary flow and transverse velocity components develop. These features modify the local shear distribution and may enable additional instability mechanisms that are not present in the 2D infinite span configuration.

To characterize these effects, a Generalized Inflection-Point (GIP) analysis is performed. In compressible boundary layers, inviscid inflectional susceptibility can be assessed using the density-weighted shear:

$$\rho \frac{dU_t}{dn}, \tag{9}$$

where U_t denotes the local tangential velocity component along the considered shear direction and n is the coordinate normal to that shear layer. In the classical GIP formulation, inflectional locations correspond to zero-crossings of the gradient of this quantity,

$$\frac{d}{dn}\left(\rho \frac{dU_t}{dn}\right) = 0. \tag{10}$$

In the present work, GIP locations are inferred from local extrema. The GIP distribution along the sidewalls is shown in Figs. 20-21, for the streamwise and transverse velocity components, respectively. These provide a necessary condition for inviscid instability and are used here as indicators of regions susceptible to disturbance growth.

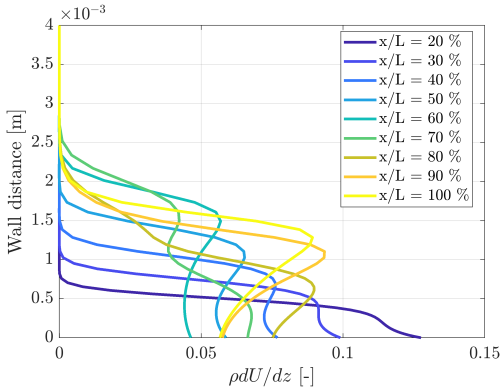


Fig. 20 GIP distribution along the sidewall, highlighting inflectional structures associated with first-mode amplification.

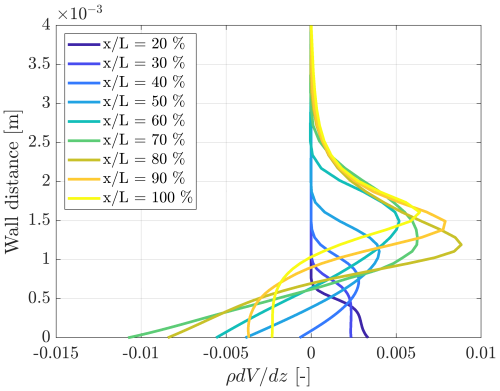


Fig. 21 GIP distribution along the sidewall, highlighting inflectional structures associated with crossflow-driven amplification.

In the upstream region, inflectional structures remain predominantly aligned with the streamwise direction, consistent with a first-mode amplification mechanism. Further downstream, additional inflectional structures emerge in regions characterized by significant transverse velocity components, indicating the onset of crossflow-driven instabilities within the boundary layer.

Overall, the sidewall boundary layer remains susceptible to inflectional instabilities throughout the nozzle, with a progressive shift in the dominant amplification mechanism from streamwise-aligned shear layers upstream to crossflow-induced shear layers downstream. In the intermediate region, both mechanisms may coexist, leading to disturbances with a mixed character reflecting the evolving shear structure.

These observations motivate the need for a stability analysis of the sidewall boundary layer, which is performed in the following section using LST and LPSE.

5.3 Stability Analysis of the Three-Dimensional base flow

To verify the instability mechanisms identified through the GIP analysis and to assess the robustness of the two-dimensional optimization, a stability analysis is performed on boundary-layer profiles extracted from the three-dimensional base flow.

The analysis follows a two-step approach. LST is first employed to rapidly identify the dominant instability modes and their amplification. Linear Parabolized Stability Equations (LPSE) are then applied to account for the expected non-parallel and non-local effects arising from the streamwise evolution and spanwise non-uniformity of the boundary layer. This enables a more accurate characterization of the instability development by relaxing the local parallel flow assumptions inherent to LST.

5.3.1 Top-wall stability assessment

The top-wall boundary layer is analyzed both on the symmetry plane (z=0.05 m) and at an off-symmetry spanwise plane (z=0.025 m), enabling a direct comparison with the original two-dimensional predictions and an evaluation of spanwise variations. For

consistency, the same frequency and spanwise wavenumber ranges used in the two-dimensional analysis, defined in Section 3.3, are considered in following computations.

Figure 22 shows the streamwise evolution of the N-factor along the top wall, comparing the two-dimensional reference results with those obtained from the three-dimensional base flow at different spanwise locations.

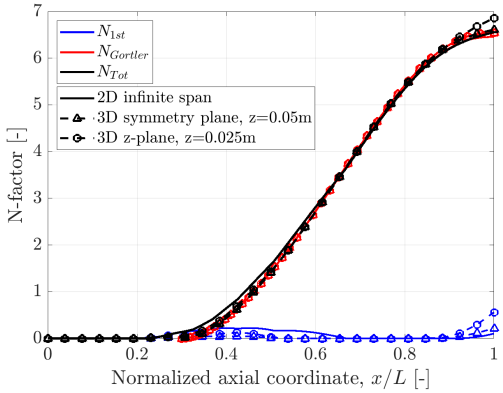


Fig. 22 Streamwise evolution of the N-factor along the top wall. Comparison between two-dimensional stability results and three-dimensional base flow predictions at different spanwise locations (symmetry plane and off-symmetry position). Contributions from first-mode and Görtler instabilities are also shown.

A good agreement is observed between the two-dimensional and three-dimensional results, with relative errors in overall amplification remaining below 5%. Both the global amplification and the individual contributions of first-mode and Görtler instabilities remain largely unchanged across spanwise locations. The first-mode amplification exhibits only minor downstream deviations, with a N-factor increase of 0.3, while the Görtler instability remains essentially unaffected. These results suggest that, despite the three-dimensional distortion of the base flow, the stability characteristics of the top-wall boundary layer are largely preserved. The dominant mechanisms and their cumulative amplification remain consistent with 2D predictions, indicating that the two-dimensional optimization provides a reliable first-order approximation for top-wall stability in the present configuration.

A comparison between LST and LPSE predictions along the top wall at the symmetry plane is presented in Fig. 23, following the ΔN methodology introduced by Testa et al. [21]. In this framework, the relative correction is defined as the difference between the N-factor predicted by LPSE and that obtained by LST, evaluated at the nozzle exit, i.e. $\Delta N = N_{\mathrm{LPSE}} - N_{\mathrm{LST}}$. Individual LPSE contributions are obtained through a normalized decomposition of the perturbation fields [28], enabling a quantitative assessment of stabilizing and destabilizing non-local effects.

The results show a distinction between instability mechanisms. The first mode is consistently damped when non-local effects are included, showing thus negative ΔN contributions across all perturbation components. In contrast, Görtler instability

exhibits a more complex and component-dependent response, with both stabilizing and destabilizing contributions depending on the considered perturbation field. Overall, these findings indicate that non-local effects tend to reduce first-mode amplification, while their influence on Görtler instability is governed by the interplay between different perturbation components. Despite these differences, the resulting differences remain moderate (< 0.5 N factor), supporting the use of LST as a reliable approximation of the dominant stability behavior for the present configuration.

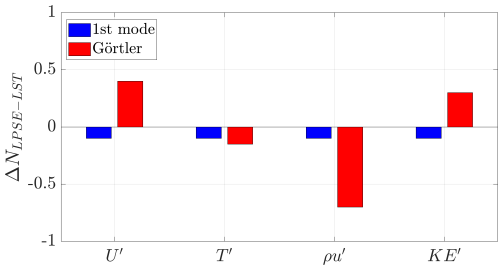


Fig. 23 LST vs LPSE results comparison for each instability mechanism.

5.3.2 Side-wall stability assessment

Consistent with the GIP analysis, the sidewall boundary layer is expected to evolve from a first-mode-dominated regime in the upstream region to a regime where crossflow-driven instability mechanisms become significant further downstream, as the flow evolves past the nozzle inflection region and progressively expands toward the uniform core flow.

To investigate this behaviour, a two-step stability analysis is performed. In the first step, a stability map is constructed over the entire sidewall by performing local LST computations along a set of 30 inviscid streamlines spanning the vertical direction from the centerline to the wall, visible in Figure 24. This approach enables the identification of dominant instability regions and their spatial distribution.

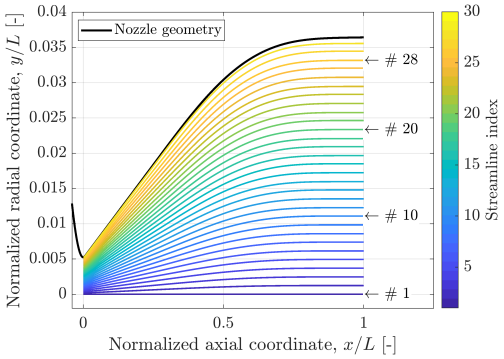


Fig. 24 Set of 30 inviscid streamlines used as computational path for linear stability analyses.

Due to the strong three-dimensional nature of the sidewall flow, including the presence of secondary vortical structures and non-parallel effects, the definition of a unique integration path for N-factor evaluation becomes ambiguous. For this reason, the analysis focuses *primarily* on local growth-rate distributions rather than integrated amplification, allowing a consistent comparison between the reference and optimized configuration.

For the sidewall stability analysis, a parametric study was conducted over a frequency range of $f \in [0, 15]$ kHz and a wide spanwise wavenumber range β=[0.005 0.075], without prior assumptions on the dominant wavelength due to the absence of established reference values for this configuration. Disturbances are characterized by a spanwise wavenumber defined as

$$\beta = \frac{2\pi}{\lambda_z},$$

where λ_z denotes the spanwise wavelength along the sidewall direction.

Figure 25 presents the growth-rate maps along nozzle sidewall for three different configurations, namely the reference case, the optimized configuration with the optimal spatially varying wall temperature $T_w(x)$, and the optimized configuration with isothermal wall temperature ($T_w = 300$ K). The contour maps are constructed by selecting, at each streamwise location, the maximum amplification rate over the explored β range at a representative frequency of $f = 12$ kHz. This frequency is selected as it consistently exhibits among the highest amplification levels across the explored parameter space and is therefore representative of the dominant instability behaviour in the sidewall boundary layer.

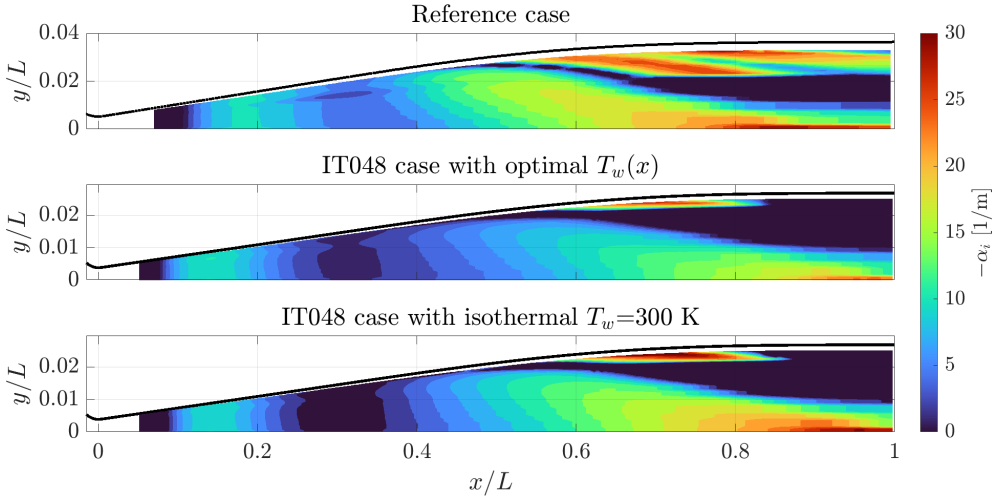


Fig. 25 Sidewall local growth-rate distribution for the reference configuration. The map represents the maximum amplification rate over the explored β range at $f = 12$ kHz.

The results indicate strong amplification of disturbances along the sidewall for all configurations. In the upstream region (approximately $x/L = 0.1$–0.2), the instability is primarily associated with first-mode mechanisms, whereas further downstream a distinct amplification pattern develops, characterized by spatially localized regions of high growth. This behaviour is consistent with crossflow instability, which becomes dominant beyond the nozzle inflection point and exhibits a clustered distribution along the sidewall.

A comparison between the three configurations reveals a clear reduction in amplification levels for both optimized configurations relative to the reference case, indicating an overall stabilizing effect resulting from the combined influence of geometric modification and wall thermal conditions. A more detailed comparison between the two optimized configurations allows these effects to be partially disentangled: the isothermal case isolates the influence of geometry, while the configuration with optimized $T_{\mathrm{w}}(x)$ highlights the additional contribution of thermal control. The results show that the optimized wall temperature distribution further reduces instability growth rates, not only in the upstream first-mode-dominated region but also, to a lesser extent, in the downstream crossflow-dominated structures.

This observation indicates that thermal control strategies, although primarily designed to mitigate 2D instability mechanisms, can also influence three-dimensional instability development. In particular, the attenuation of crossflow amplification suggests that wall temperature optimization may provide an effective pathway for reducing sidewall transition in configurations characterized by strong three-dimensional effects. This behavior is consistent with variations in the GIP, as changes in wall temperature directly affect its location across the boundary layer.

To complement the local growth-rate maps with an indicative transition-risk estimate, streamline-based N-factors are evaluated along a fixed family of representative sidewall-adjacent streamlines using identical extraction and integration procedures and shown in Fig. 26.

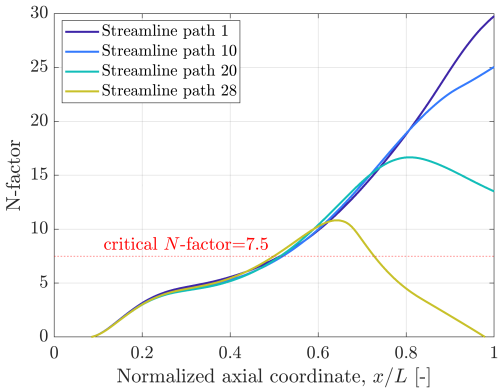


Fig. 26 Streamline-based N-factor evolution along a fixed family of representative sidewall-adjacent streamlines. Because N-factor integration in a strongly three-dimensional boundary layer is path-dependent, these curves are interpreted as a range of transition risk rather than a unique prediction of the transition location.

Although a unique integration path is not defined in a strongly three-dimensional sidewall boundary layer, reporting $N(x)$ over a prescribed streamline family provides a consistent *comparative diagnostic* and enables a range-based estimate of transition risk. For the present configuration, the conventional threshold ($N_{\mathrm{crit}} = 7.5$) is reached around $x/L \approx 0.5$ (with variability across streamlines shown in Fig. 26), indicating that sidewall transition may occur upstream of the intended uniform core region.

In a second step, LPSE are employed to relax the assumptions of local parallel flow and to assess the influence of non-parallel and non-local effects. Calculations are performed along selected streamlines to evaluate the robustness of the LST predictions when streamwise non-parallelism of the base flow is taken into account.

A comparison between LST and LPSE predictions is shown in Fig. 27. Overall, a good agreement is observed, up to LPSE computation termination, confirming that LST provides a consistent first-order description of the dominant instability mechanisms.

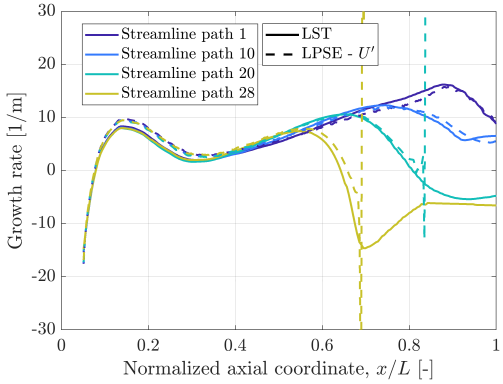


Fig. 27 Comparison between LST and LPSE growth-rate predictions along selected streamlines. Solid lines: LST; dashed lines: LPSE. Vertical dashed lines indicate termination of LPSE integration due to violation of underlying assumptions.

In the upstream region, where first-mode disturbances dominate, LPSE predicts slightly higher growth rates, reflecting non-parallel effects not captured by the local framework. Further downstream, where crossflow-type instabilities become dominant, the agreement between the two approaches improves, with both theories consistently identifying the location and extent of the amplification region.

Along near-wall and intermediate streamlines (streamlines path #28, 20 and 10), the LPSE integration terminates shortly downstream of the main amplification region. This behaviour reflects a fundamental limitation of the marching formulation: the strong three-dimensionality of the base flow and the presence of rapid streamwise variations violate the assumption of slowly varying disturbances. As a result, LPSE is no longer able to sustain downstream integration, while LST, being local, remains applicable across the full domain.

The termination of LPSE integration thus provides a direct indication of where its underlying assumptions break down. In these regions, the local, quasi-two-dimensional

description of the flow becomes insufficient, and linear two-dimensional stability theories can no longer be fully relied upon. Taken together, this comparison delineates the domain of validity of the two approaches: LPSE offers improved fidelity where the base flow evolves slowly, whereas LST remains applicable in strongly non-parallel regions, albeit with reduced physical accuracy. The breakdown of LPSE integration thus marks the limits of weakly non-parallel formulations and identifies regions where higher-fidelity approaches are required.

In regions where these limitations become significant, more advanced formulations are required to accurately capture the instability dynamics, such as plane-marching PSE [42, 43] or spanwise BiGlobal stability theory (also known as 2D LST) [44] analyses performed on streamwise planes.

6 Conclusions

This work developed and applied a stability-based optimization framework for the design of planar supersonic nozzles, targeting a prescribed exit Mach number ($M = 3.5$) and quiet Reynolds number ($Re_{\Delta x} \approx 20 \times 10^6$). The optimization methodology is formulated within a two-dimensional framework, combining inviscid contour generation, boundary-layer computation feeding nozzle geometry viscous correction, and linear stability theory within a Bayesian optimization loop. This approach enables efficient identification of configurations that minimize disturbance amplification along the nozzle walls.

The optimization results demonstrate that it is possible to maintain subcritical amplification levels ($N_{\text{combined}} < 7.5$) along the top wall while satisfying the target operating conditions, in contrast with the reference configuration which predicts early transition. Beyond this quantitative improvement, the analysis provides clear physical design guidelines. In particular, low values of the opening angle ω and of the straightening length X_{BC} consistently reduce Görtler instability growth by limiting centrifugal effects and the extent of concave flow regions. The optimized wall-temperature distribution emerges as a key control parameter: it features elevated temperatures in the throat region followed by a sharp drop at approximately 30% of the nozzle length, which effectively damp first-mode instability, and a moderated increase toward the exit. This distribution at nozzle exit reflects a fundamental trade-off, as higher exit temperatures attenuate Görtler modes through viscous–geometric effects while simultaneously promoting first-mode amplification, whereas lower temperatures have the opposite effect. The optimal solution balances these competing mechanisms and limits their spatial overlap.

The robustness of the optimized 2D design was assessed through three-dimensional simulations including sidewall effects. Along the top wall, the agreement with two-dimensional predictions remains excellent (relative differences below 5%), confirming that the 2D infinite span optimization framework provides a reliable first-order description in regions where the flow retains a quasi-two-dimensional character.

In contrast, the sidewall boundary layer exhibits strong three-dimensionality induced by anisotropic expansion and secondary flow structures. These effects introduce transverse velocity components in boundary-layer low momentum regions and

thus inflectional shear layers, leading to crossflow-type instabilities that are not captured in the 2D framework. Local growth-rate analyses show consistently large amplification levels across both reference and optimized configurations. A complementary N-factor assessment along representative inviscid streamlines indicates that the transition threshold may be reached as early as $x/L \approx 0.5$, suggesting that sidewall-induced transition can occur upstream of the intended quiet-flow region even for the optimized geometry.

A key outcome of this study is that the optimized wall-temperature distribution, although derived within a two-dimensional framework, also attenuates crossflow amplification along the sidewalls. This demonstrates that thermal control can influence inherently three-dimensional instability mechanisms, revealing a previously underexplored coupling and providing a new design lever for mitigating sidewall transition.

The comparison between LST and LPSE further clarifies the range of validity of linear stability predictions. In the upstream region, where the base flow evolves gradually, both approaches provide consistent results and can be reliably applied. Further downstream, increasing non-parallelism and three-dimensionality lead to the breakdown of LPSE marching approach, marking the limit of weakly non-local/non-parallel formulations. This behaviour delineates the practical envelope of confidence of linear, quasi-two-dimensional stability analyses.

Overall, the present study demonstrates that stability-based optimization constitutes an effective and physically interpretable tool for controlling top-wall transition in planar nozzles, while simultaneously identifying the key geometric and thermal design levers governing instability growth. At the same time, it establishes that sidewall-induced three-dimensional effects can dominate the transition process and must be explicitly accounted for in realistic configurations. Accurately capturing these mechanisms requires higher-fidelity approaches capable of resolving multidirectional instability dynamics, such as plane-based stability analyses or nonlinear formulations. Integrating such approaches within the design framework represents a critical step toward predictive and robust quiet nozzle design under fully three-dimensional flow conditions.

Acknowledgements. The authors gratefully acknowledge Dr. M. Capriati and V. Romano for valuable discussions on the interpretation of the results and the implementation of the optimization framework. The authors also thank A. Ghyoot for the contribution to the development of an efficient meshing toolkit for nozzle geometries.

Declarations

- **Funding:** This work was supported by the European Space Agency (ESA) under contract No. 4000139380.
- **Conflict of interest:** Author J. Steelant serves as a Managing Editor of CEAS Space Journal. J. Steelant was not involved in the editorial handling, peer review, or decision-making process for this manuscript. The remaining authors declare no competing interests.
- **Consent for publication:** Not applicable.

- **Data availability:** The datasets generated and/or analysed during the current study are not publicly available.
- **Materials availability:** Not applicable.
- **Code availability:** The code used in this study is not publicly available.
- **Author contributions:** All authors contributed to the study conception and design. Material preparation, data collection, and analysis were performed by A. Testa. The first draft of the manuscript was written by A. Testa, and all authors commented on previous versions of the manuscript. All authors read and approved the final manuscript.

References

[1] Schneider, S.P.: Effects of high-speed tunnel noise on laminar-turbulent transition. Journal of Spacecraft and Rockets **38**(3), 323–333 (2001) https://doi.org/10.2514/2.3705

[2] Laufer, J.: Aerodynamic noise in supersonic wind tunnels. Journal of the Aerospace Sciences **28**, 685–692 (1961)

[3] Morkovin, M.V.: On transition experiments at moderate supersonic speeds. Journal of the Aeronautical Sciences **24**(7), 480–486 (1957) https://doi.org/10.2514/8.3887

[4] Pate, S.R.: Effects of wind tunnel disturbances on boundary-layer transition with emphasis on radiated noise: A review. 11th AIAA Aerodynamic testing conference (1980)

[5] Casper, K., Johnson, H., Schneider, S., Danehy, P., Horvath, T., Resothko, E., Choudhari, M., Reed, H.: Effect of freestream noise on roughness-induced transition for a slender cone. Journal of Spacecraft and Rockets **48**, 406–413 (2011) https://doi.org/10.2514/1.48300

[6] Lin, T.: Influence of laminar boundary-layer transition on entry vehicle designs. Journal of Spacecraft and Rockets **45**, 165–175 (2008) https://doi.org/10.2514/1.30047

[7] van Driest, E.R.: The problem of aerodynamic heating. Aeronautical Engineering Review **15**(10), 26–41 (1956)

[8] Chazot, O., Gülhan, A., Hannemann, K., McGilvray, M., Serre, L., Tran, P., Steelant, J.: Need for Low-Noise High-Speed Facilities in Europe. International Conference on Flight vehicles, Aerothermodynamics and Re-entry Missions and Engineering (FAR) (2019)

[9] Beckwith, I.E., Holley, B.B.: Gortler vortices and transition in wall boundary layers of two mach 5 nozzles. In: Technical Report NASA TP-1869, National

Aeronautics and Space Administration (1981)

[10] Görtler, H.: On the three-dimensional instability of laminar boundary layers on concave walls. Technical Report NACA TM 1375 (1954)

[11] Saric, W.S.: Görtler vortices. Annual Review of Fluid Mechanics **26**, 379–409 (1994) https://doi.org/10.1146/annurev.fl.26.010194.002115

[12] Floryan., J.M.: On the Görtler instability of boundary layers. Progress in Aerospace Sciences **28**(3), 235–271 (1991)

[13] Chen, F.-J., Malik, M., Beckwith, I.: Instabilities and transition in the wall boundary layers of low-disturbance supersonic nozzles. In: 18th Fluid Dynamics and Plasmadynamics and Lasers Conference. https://doi.org/10.2514/6.1985-1573

[14] Schmid, P.J., Henningson, D.S.: Stability and Transition in Shear Flows. Springer, New York (2012)

[15] Schneider, S.: Design of a mach-6 quiet-flow wind-tunnel nozzle using the e**n method for transition estimation. In: 36th AIAA Aerospace Sciences Meeting and Exhibit. https://doi.org/10.2514/6.1998-547

[16] Schneider, S.: The development of hypersonic quiet tunnels. Journal of Spacecraft and Rockets **45**, 641–664 (2008) https://doi.org/10.2514/1.34489

[17] Demetriades, A.: Stabilization of a nozzle boundary layer by local surface heating. AIAA Journal **34**(12), 2490–2495 (1996) https://doi.org/10.2514/3.13429

[18] Lakebrink, M., Bowcutt, K., Winfree, T., Huffman, C., Juliano, T.: Optimization of a mach-6 quiet wind-tunnel nozzle. Journal of Spacecraft and Rockets **55**, 1–7 (2017) https://doi.org/10.2514/1.A33794

[19] Jones, D., Schonlau, M., Welch, W.: Efficient global optimization of expensive black-box functions. Journal of Global Optimization **13**, 455–492 (1998) https://doi.org/10.1023/A:1008306431147

[20] Lemarquand, H., Lugrin, M., Content, C., Caillaud, C., Esquieu, S., Sipp, D.: Transition mechanisms in hypersonic wind-tunnel nozzles: a methodological approach using global linear stability analysis. Flow **5**, 42 (2025) https://doi.org/10.1017/flo.2025.10033

[21] Testa, A., Schrooyen, P., Grossir, G., Steelant, J.: Advanced design methodology for laminar boundary layer control in axisymmetric nozzles. 11th European Conference for AeroSpace Sciences (EUCASS) (2025). https://doi.org/10.13009/EUCASS2025-504

[22] Grossir, G., Chazot, O.: Design of axisymmetric contoured nozzles for calorically

and thermally imperfect gases using the Hypnoze code. In HiSST: 2nd International Conference on High-Speed Vehicle Science & Technology, HiSST-2022-0038. (2022)

[23] Miró Miró, F., Groot, K., Beyak, E.S., Moyes, A.J., Pinna, F., Reed, H.L.: DEKAF: an open-source spectral boundary-layer solver. Tech. Rep. VKI-TM-56, von Karman Institute for Fluid Dynamics (2020)

[24] Sivells, J.C.: Aerodynamic design of axisymmetric hypersonic wind tunnel nozzles. Journal of Spacecraft and Rockets **7**(11), 1292–1299 (1970)

[25] Pinna, F.: Numerical study of stability of flows from low to high Mach number. PhD thesis, von Karman Institute for Fluid Dynamics - Universitá di Roma "La Sapienza" (2012)

[26] Mack, L.M.: Boundary layer linear stability theory. In Special course on stability and transition of laminar flows, von Karman Institute for Fluid Dynamics (1984)

[27] Saric, W., Reed, H., White, E.: Stability and transition of three-dimensional boundary layers. Annual Review of Fluid Mechanics **35**, 413–440 (2003) https://doi.org/10.1146/annurev.fluid.35.101101.161045

[28] Herbert, T.: Parabolized stability equations. Annual Review of Fluid Mechanics **29**, 245–283 (1997) https://doi.org/10.1146/annurev.fluid.29.1.245

[29] Smith, A.M.O., Gamberoni, N.: Transition, pressure gradient and stability theory. Technical Report ES-26388, Douglas Aircraft Co. (1956)

[30] Ingen, H.L.: A suggested semi-empirical method for the calculation of the boundary layer transition region, technical report vth-74. Technical report, Technische Hogeschool Delft, Vliegtuigbouwkunde (1956)

[31] Brochu, E., Cora, V.M., Freitas, N.: A Tutorial on Bayesian Optimization of Expensive Cost Functions, with Application to Active User Modeling and Hierarchical Reinforcement Learning (2010). https://arxiv.org/abs/1012.2599

[32] McKay, M.D., Beckman, R.J., Conover, W.J.: A comparison of three methods for selecting values of input variables in the analysis of output from a computer code. Technometrics **21**(2), 239–245 (1979)

[33] Rasmussen, C., Williams, C.: Gaussian Processes for Machine Learning, (2005). https://doi.org/10.7551/mitpress/3206.001.0001

[34] Beckwith, I.E.: Development of a high reynolds number quiet tunnel for transition research. AIAA Journal **13**(3), 300–306 (1975) https://doi.org/10.2514/3.49695

[35] Beckwith, I., Chen, F.-J., Malik, M.: Design and fabrication requirements for low-noise supersonic/hypersonic wind tunnels. 26th Aerospace Sciences Meeting.

https://doi.org/10.2514/6.1988-143

[36] Sivells, J.C.: A Computer Program for the Aerodynamic Design of Axisymmetric and Planar Nozzles for Supersonic and Hypersonic Wind Tunnels. Tech. Rep. AEDC-TR-78-63, Arnold Engineering Development Center (1978)

[37] Stone, M.: Cross-validatory choice and assessment of statistical predictions. Journal of the Royal Statistical Society. Series B (Methodological) **36**(2), 111–147 (1974)

[38] Sobol, I.M.: Global sensitivity indices for nonlinear mathematical models and their Monte Carlo estimates. Mathematics and Computers in Simulation **55**(1-3), 271–280 (2001)

[39] Kohonen, T.: Self-organized formation of topologically correct feature maps. Biological Cybernetics **43**(1), 59–69 (1982)

[40] Metacomp Technologies Inc.: CFD++: Computational Fluid Dynamics Software. https://www.metacomptech.com. Version 18.1 (2023)

[41] Sabnis, K., Babinsky, H.: Nozzle geometry effects on corner boundary layers in supersonic wind tunnels. AIAA Journal **57**, 1–4 (2019) https://doi.org/10.2514/1.J058310

[42] Paredes, P., Hanifi, A., Theofilis, V., Henningson, D.S.: The nonlinear pse-3d concept for transition prediction in flows with a single slowly-varying spatial direction. Procedia IUTAM **14**, 36–44 (2015) https://doi.org/10.1016/j.piutam.2015.03.021 . IUTAM ABCM Symposium on Laminar Turbulent Transition

[43] Ambrosino, B., Tocci, F., Theiß, A., Hein, S., Rodríguez, D.: Stationary crossflow vortices' secondary instability: Linear stability theory and parabolized stability equations. AIAA Journal **63**(6), 2182–2198 (2025) https://doi.org/10.2514/1.J064663

[44] Groot, K.J., Serpieri, J., Pinna, F., Kotsonis, M.: Secondary crossflow instability through global analysis of measured base flows. Journal of Fluid Mechanics **846**, 605–653 (2018) https://doi.org/10.1017/jfm.2018.253